Compaction front and pore fluid pressurization in horizontally shaken drained granular layers

Shahar Ben Zeev, Einat Aharonov, Renaud Toussaint, Stanislav Parez, Liran Goren

Compaction front and pore fluid pressurization in horizontally shaken drained granular layers

Shahar Ben-Zeev,[1,2,*] Einat Aharonov,[1] Renaud Toussaint,[2,3] Stanislav Parez,[4] and Liran Goren[5]

[1] *Institute of Earth Science, Hebrew University of Jerusalem, Israel*
[2] *Université de Strasbourg, CNRS, Institut de Physique du Globe de Strasbourg, UMR7516, F-67000 Strasbourg, France*
[3] *PoreLab, the Njord Center, Physics Department, University of Oslo, Oslo, Norway*
[4] *Institute of Chemical Process Fundamentals of the CAS, Prague, Czech Republic*
[5] *Geological and Environmental Science, Ben-Gurion University of the Negev, Israel*

(Dated: March 5, 2020)

In many natural granular systems, the interstitial pores are filled with a fluid. Deformation of this two-phase system is complex, highly coupled, and depends on the initial and boundary conditions. Here we study granular compaction and fluid flow in a saturated, horizontally shaken, unconfined granular layer, where the fluid is free to flow in and out of the layer through the free upper surface during shaking (i.e., drained boundary condition). The geometry, boundary conditions and parameters are chosen to resemble a shallow soil layer, subjected to horizontal cyclic acceleration simulating that of an earthquake. We develop a theory and conduct coupled discrete element and fluid numerical simulations. Theoretical and simulation results show that under drained conditions and above a critical acceleration, the grain layer compacts at a rate governed by the fluid flow parameters of permeability and viscosity, and is independent of the shaking parameters of frequency and acceleration. A compaction front develops, swiping upward through the system. Above the front, compaction occurs and the fluid becomes pressurized. Pressure gradients drive fluid seepage upward and out of the compacting layer while supporting the granular skeleton. The rate of compaction and the interstitial fluid pressure gradient coevolve until fluid seepage forces balance solid contact forces and grain contacts disappear. As an outcome, the imposed shear waves are not transmitted and the region is liquefied. Below the compaction front (i.e., after its passage), the grains are well compacted, and shaking is transmitted upward. We conclude that the drained condition for the interstitial pore fluid is a critical ingredient for the formation of an upward moving compaction front, which separates a granular region that exhibits a liquid-like rheology from a solid-like region.

I. INTRODUCTION

Deformation of densely packed granular media is a subject of great complexity with applications ranging from industry to natural hazards. In particular, the mechanics of shearing granular media has been shown to control earthquakes (e.g., [1–5]), lead to soil liquefaction (e.g., [6–8]) and control the initiation and movement of landslides (e.g., [9–14]). Granular shear exhibits rich and not well understood behavior even when the grain layers are dry [15–22]. The deformation becomes more complicated when a viscous fluid is present in the pore space between grains, as occurs in most geological systems (e.g., [7, 23, 24]). Interstitial pore fluid may greatly affect granular deformation because shear deforms the granular skeleton, causing pore space compaction and dilation [25–27]. These porosity variations lead to pore pressure changes [28], that drive fluid flow [24], and feed back into the granular deformation by imposing forces on grains [29]. These coupled interactions have been studied in various geometrical settings, including continuous horizontal shear under imposed normal stresses [25, 30–33], compaction and decompaction due to fluid flow [34, 35], vertical discrete tapping [36], impacting intruder [37], vertical continuous shaking [38] and cyclic horizontal shear [8, 39] of a horizontally confined layer.

Here, we aim to study the coupled interactions between grains and interstitial pore fluid in a setting that corresponds to saturated soils undergoing earthquake shaking. The soil is represented as a horizontally unconfined layer, with a finite thickness and a free surface at the top. The fluid fully occupies the pore space in the layer. The earthquake shaking is represented as horizontal cyclic shear at accelerations that are well below the gravitational acceleration. In this paper, we will use the terms "cyclic shear" and "horizontal shaking" interchangeably, to describe this boundary condition.

Natural soils under low overburden stresses, as exist at the shallow subsurface, tend to compact during cyclic shear [40]. We expect that when a viscous interstitial fluid is present, compaction will be accompanied by fluid outflow and pressurization [38]. Here, the fluid drainage conditions (i.e. its ability to flow in and out of the layer), have a key role in controlling both the grain layer dynamics and the fluid pressure and flow. It is usually believed that during the rapid shaking that characterizes earthquakes, fluid cannot drain out of the layer and hence fluid flow does not play an important role in the development of pore pressure, and in the compaction process [7]. However, recently it has been suggested [24, 33, 39, 41, 42] that even during rapid cyclic shearing, upward fluid flow may be crucial for the coupled deformation, motivat-

* shahar.benzeev@mail.huji.ac.il

ing a re-evaluation of the effect of fluid flow on pressure changes and compaction during horizontal cyclic shear.

A critical application of the geometry and dynamics that we study here is the hazardous natural phenomenon called "soil liquefaction", which is often triggered by earthquakes. During liquefaction, soils exhibit an abrupt rheological change where they transition from elastoplastic stress-supporting solid layers to a liquid-like granular phase that flows easily under small applied shear stresses [43, 44]. Observations indicate that liquefaction is associated with soil compaction and settlement [45], and pore fluid pressurization is considered as a major driving mechanism for this rheological change [40]. The coupled dynamics that emerge from our idealized shaken saturated grain layer is thus highly relevant to the process of liquefaction.

In the following, we develop a theory for such systems, i.e., unconfined saturated grain layers subjected to horizontal cyclic shear. We establish the conditions under which the proximity to the surface allows fluid to flow in and out of the layer during the imposed deformation, namely, when the grain layer is effectively well-drained. These drainage conditions impose a particular form of fluid-grains coupling. We then present a numerical Discrete Element Method (DEM) and Computational Fluid Dynamics (CFD) framework to study the coupling between compacting grains and fluid flow and pressurization. The agreement between simulation results and theory allows us to present a fully consistent framework of drained granular dynamics in response to cyclic horizontal shaking.

II. GRAIN-FLUID COUPLING UNDER DRAINED CONDITIONS

To identify the dominant interactions between a compacting grain layer and the interstitial fluid flow and pressurization, we develop a theory for the pore fluid response to a general deformation of the grain skeleton. Previous general formulations [24, 33] are adopted to the setting of a shallow saturated soil column: The non-dimensional analysis is tailored for low stresses with respect to the fluid bulk modulus. Based on this analysis, the dominant interactions under well-drained conditions are identified.

We start with mass conservation equations over representative elementary volume for the solid (Eq. (1)) and the fluid (Eq. (2)) phases:

$$\frac{\partial[(1-\phi)\rho_s]}{\partial t} + \nabla\cdot[(1-\phi)\rho_s \boldsymbol{u_s}] = 0 \tag{1}$$

$$\frac{\partial[\phi\rho_f]}{\partial t} + \nabla\cdot[\phi\rho_f \boldsymbol{u_f}] = 0, \tag{2}$$

where ρ_s and ρ_f are the solid and fluid material densities, respectively, ϕ is the porosity, $\boldsymbol{u_s}$ and $\boldsymbol{u_f}$ are the solid grain and fluid velocities, respectively, and t stands for time (vectors are represented by bold fonts). Grains are assumed incompressible with respect to the pore fluid. This assumption is valid for example for quartz grains and interstitial water with compressibilities of $2.7\cdot10^{-11}$ Pa^{-1} and $4.5\cdot10^{-10}$ Pa^{-1}, respectively. With this assumption, Eq. (1) is rewritten as:

$$\frac{\partial\phi}{\partial t} = \nabla\cdot[(1-\phi)\boldsymbol{u_s}]. \tag{3}$$

Further assuming that fluid inertia is negligible compared to the viscous forces, the fluid momentum equation reduces to Darcy flux law [46]. When the solid grain skeleton is deformable, this law is expressed as:

$$\phi(\boldsymbol{u_f} - \boldsymbol{u_s}) = -\frac{\kappa}{\eta}\boldsymbol{\nabla} P', \tag{4}$$

where κ is the permeability, η the fluid dynamic viscosity and P' the fluid pressure deviation from hydrostatic values such that $\boldsymbol{\nabla} P' = \boldsymbol{\nabla} P - \rho_f \boldsymbol{g}$. The right hand side of Eq. (4) is commonly referred to as "Darcy flux". The fluid density is described by a state equation of the form:

$$\rho_f = \rho_{f,0}(1+\beta P'), \tag{5}$$

where $\rho_{f,0}$ the fluid density under hydrostatic conditions, with atmospheric pressure on top, and $\beta = (1/\rho_f)(\partial\rho_f/\partial P)$ is the adiabatic fluid compressibility. Next we assess the magnitude of $\beta P'$ in Eq. (5) for the shallow, saturated and cohesionless soil layer considered here. The pore water compressibility is $O(10^{-10})$ Pa^{-1}, and P' cannot significantly exceed the value of effective static normal stress. To evaluate its value we assume the top of the water column is exactly at the surface, and consider a reference case without dynamic pressure:

$$\begin{aligned}\sigma_0 &= \rho_{\text{eff}} g y - \rho_f g y \\ &= [(1-\phi)\rho_s + \phi\rho_f - \rho_f] g y \\ &= (1-\phi)(\rho_s - \rho_f) g y,\end{aligned} \tag{6}$$

where ρ_{eff} is the effective density of a saturated porous layer and y is the downward vertical coordinate, zeroed at the surface. In Eq. (6), σ_0 increases with depth and its maximal value within a vertically finite domain occurs at depth h, the base of the domain, $\sigma_0^h = \sigma_0(y=h)$. For a layer with quartz grains ($\rho_s = 2640$ kg m^{-3}) that extends down to 1 km (much deeper than the systems we consider here), $\sigma_0^h \lesssim O(10^7)$ Pa, and therefore $\beta P' \ll 1$ and:

$$(1+\beta P') \approx 1. \tag{7}$$

Multiplying Eq. (3) by ρ_f, subtracting it from Eq. (2), and combining with Eqs. (4), (5) and (7) leads to:

$$\phi\beta\frac{\partial P'}{\partial t} + \phi\beta\boldsymbol{u_s}\cdot\boldsymbol{\nabla} P' - \nabla\cdot[\frac{\kappa}{\eta}\boldsymbol{\nabla} P'] + \nabla\cdot\boldsymbol{u_s} = 0. \tag{8}$$

In Eq. (8), the first term describes the temporal derivative of the dynamic pore fluid pressure, the second term

describes dynamic pore pressure advection, the third term is the dynamic pore pressure laplacian, corresponding to the divergence of the Darcy flux, and the last term describes the effect of the granular skeleton deformation on the fluid pressure via compaction and dilation.

The relative importance of the different terms in Eq. (8) is evaluated using a non-dimensional analysis. We choose the system height, h, as the length scale such that $\nabla = \hat{\nabla}/h$, where the symbol $\hat{}$ denotes non-dimensional operators and variables. The time and permeability scale factors are t_0 and κ_0, respectively, such that $t = \hat{t}t_0$ and $\kappa = \hat{\kappa}\kappa_0$. The pore pressure is scaled with the maximum effective static normal stress as $P' = \hat{P}'\sigma_0^h$. The velocity scale factor $u_0 = (\kappa_0\sigma_0^h)/(\phi\eta h)$, is chosen based on Darcy's flux (Eq. 4) when $\nabla P' = \nabla\sigma_0 = \sigma_0^h/h$, such that $\boldsymbol{u_s} = \hat{\boldsymbol{u}}_{\boldsymbol{s}}u_0$. This choice reflects our expectations for the importance of fluid flow in our system. In other settings, where fluid flow is vanishingly small with respect to the rate of deformation, a different velocity scale factor should be used [24, 33]. Following these definitions, Eq. (8) becomes:

$$\frac{\partial\hat{P}'}{\partial\hat{t}} + \frac{\kappa_0 t_0\sigma_0^h}{\phi\eta h^2}\hat{\boldsymbol{u}}_{\boldsymbol{s}}\cdot\hat{\boldsymbol{\nabla}}\hat{P}' - \frac{\kappa_0 t_0}{\phi\beta\eta h^2}\hat{\nabla}\cdot[\hat{\kappa}\hat{\boldsymbol{\nabla}}\hat{P}'] + \frac{\kappa_0 t_0}{\phi^2\beta\eta h^2}\hat{\nabla}\cdot\hat{\boldsymbol{u}}_{\boldsymbol{s}} = 0. \quad (9)$$

The parametric group $t_d = (h^2\beta\eta\phi)/(\kappa_0) = h^2D^{-1}$ has the meaning of a diffusion time scale over the layer depth, where $D = (\kappa_0)/(\beta\eta\phi)$ is the pore pressure diffusion coefficient. With this definition, Eq. (9) is written as:

$$\frac{\partial\hat{P}'}{\partial\hat{t}} + \frac{t_0}{t_d}\beta\sigma_0^h\hat{\boldsymbol{u}}_{\boldsymbol{s}}\cdot\hat{\boldsymbol{\nabla}}\hat{P} - \frac{t_0}{t_d}\hat{\nabla}\cdot[\hat{\kappa}\hat{\boldsymbol{\nabla}}\hat{P}'] + \frac{t_0}{t_d}\frac{1}{\phi}\hat{\nabla}\cdot\hat{\boldsymbol{u}}_{\boldsymbol{s}} = 0. \quad (10)$$

Since we focus on a setting where $\beta\sigma_0^h \ll 1$, the second term of Eq. (10) becomes negligible relative to the third and fourth terms, and Eq. (10) is approximated as:

$$\frac{t_d}{t_0}\frac{\partial\hat{P}'}{\partial\hat{t}} - \hat{\nabla}\cdot[\hat{\kappa}\hat{\boldsymbol{\nabla}}\hat{P}'] + \frac{1}{\phi}\hat{\nabla}\cdot\hat{\boldsymbol{u}}_{\boldsymbol{s}} = 0. \quad (11)$$

We choose t_0 to represent the process time scale, which in the current system relates to the deformation of the grain skeleton (the third term in Eq. (11)). A natural choice is the periodicity of the imposed cyclic shear, $t_0 = T$. The coefficient in front of the first term of Eq. (11) then becomes the Deborah number (De) [47], which is the ratio between the relaxation time scale of a system and the process time scale:

$$\mathrm{De} = \frac{t_d}{t_0} = \frac{h^2\beta\eta\phi}{t_0\kappa_0}. \quad (12)$$

Hence, Eq. (11) is written as:

$$\mathrm{De}\frac{\partial\hat{P}'}{\partial\hat{t}} - \hat{\nabla}\cdot[\hat{\kappa}\hat{\boldsymbol{\nabla}}\hat{P}'] + \frac{1}{\phi}\hat{\nabla}\cdot\hat{\boldsymbol{u}}_{\boldsymbol{s}} = 0. \quad (13)$$

When $\mathrm{De} \gg 1$ the diffusion time scale is significantly larger than the process time scale, and the pore pressure will not relax significantly during a single shaking period, leading to "undrained" conditions. When $\mathrm{De} \ll 1$ the diffusion time scale is significantly smaller than the periodicity, leading to "drained" conditions. The De number dictates the relative importance of the terms in Eq. (13). Leaving the third term aside as the source for any dynamics that originates from deformation of the grain skeleton, we note that when $\mathrm{De} \gg 1$ ("undrained"), the second term in Eq. (13) can be neglected and the temporal evolution of the pore pressure directly correlates to the overall compaction and dilation of the grains skeleton. When $\mathrm{De} \ll 1$ ("drained"), the first term in Eq. (13) becomes negligible, and Eq. (13) reduces to a Poisson type equation of the form:

$$\hat{\nabla}\cdot[\hat{\kappa}\hat{\boldsymbol{\nabla}}\hat{P}'] = \frac{1}{\phi}\hat{\nabla}\cdot\hat{\boldsymbol{u}}_{\boldsymbol{s}} \quad (14)$$

and in a dimensional form:

$$\nabla\cdot[\frac{\kappa}{\eta}\boldsymbol{\nabla}P'] = \nabla\cdot\boldsymbol{u_s}. \quad (15)$$

Integrating Eq. (15) while assuming that $\kappa \approx \kappa_0$ leads to:

$$\frac{\kappa_0}{\eta}\boldsymbol{\nabla}P' = \boldsymbol{u_s} + C(t). \quad (16)$$

Eq. (16) reveals the dominant solid-fluid coupling in the drained setting studied here. The equation predicts that the solid velocity depends linearly on the dynamic fluid pressure gradient. When combined with Eq. (4) it becomes a statement of mass conservation, where any solid flux must be compensated by an equal and opposite fluid flux. The details of this dependency in a horizontally shaken layer is the focus of the current work.

III. A COUPLED GRAIN-FLUID MODEL

A. The model

We implement a numerical model that fully couples two phases. A solid phase, which is modeled using the Discrete Element Method (DEM) [48] and a fluid phase, which is modeled as a continuum on a superimposed Eulerian grid [24, 33, 49–63]. The core functionality of the code has been verified and used in previous studies. The granular dynamics module was used in [13, 14, 16–18, 64] and the coupling with the continuum module was used in [33, 59, 60, 65].

The grains are simulated as interacting spheres using a linear elastic frictional contact model. A velocity dependent damping is added to the normal contact force, and a threshold friction law based on the ratio of tangential and normal forces between grains is considered, allowing sliding when the shear force surpasses a frictional criterion [16–18]. Grain motion is determined by

time integration of the linear (Eq. (17)) and rotational (Eq. (18)) momentum conservation equations.

$$m_i \dot{\boldsymbol{u}}_{\boldsymbol{s},i} = m_i \boldsymbol{g} - V_{\mathrm{imm},i}\rho_f \boldsymbol{g} + \Sigma_j \boldsymbol{F}_{ij} - \frac{\boldsymbol{\nabla} P' \cdot V_i}{1-\phi} \quad (17)$$

$$I_i \dot{\boldsymbol{\omega}}_{\boldsymbol{s},i} = \Sigma_j R_i \hat{\boldsymbol{n}}_{ij} \times \boldsymbol{F}_{ij}, \quad (18)$$

where $\dot{\boldsymbol{u}}_{\boldsymbol{s},i}$ and $\dot{\boldsymbol{\omega}}_{\boldsymbol{s},i}$ are the translational and rotational accelerations of grain i (dot notation indicates time derivative) and m_i and I_i are the mass and moment of inertia of grain i. In Eq. (17), the first term on the right hand side is the gravitational force, and $\boldsymbol{g}$ is the gravitatonal acceleration. The second term is buoyancy force, induced by the hydrostatic fluid pressure gradient, whose magnitude depends on the immersed volume of the grain $V_{\mathrm{imm},i}$ and the fluid density ρ_f [66]. The third term is the sum of contact forces ($\boldsymbol{F}_{ij}$) of all grains j that are in contact with grain i. The fourth term is the drag force exerted by the fluid dynamic pressure gradient ($\boldsymbol{\nabla} P'$), where V_i is the volume of grain i. In Eq. (18), R_i is the radius of grain i and $\hat{\boldsymbol{n}}_{ij}$ is a unit vector along the direction connecting the centers of grains i and j.

The evolution of the dynamic pore fluid pressure is found by an implicit numerical solver of equation (13) over a square grid, with grid spacing of two average grain diameter [24, 33, 54, 55]. Importantly, we do not a priori assume the state of drainage, and the full three-terms equation is solved.

In order to achieve a two-way coupling between the solid and the fluid phases, the grain volumes and velocities are interpolated via a bi-linear interpolation scheme into a smooth velocity ($\boldsymbol{u}_{\boldsymbol{s}}$) and porosity ($\phi$) fields on the grid. Those quantities are used for solving the fluid equation (Eq. (13)). To solve the solid grains linear momentum equation (Eq. (17)), the dynamic pore pressure gradient ($\boldsymbol{\nabla} P'$) along with the local average porosity (ϕ) are interpolated using an inverse scheme, from the grid to each grain (Fig. 1). In the model, the permeability and the porosity are related by the 3D Kozeny-Carman relationship [67]:

$$\kappa = \kappa_1 \kappa'(x,y,t) = \alpha \bar{r^2} \frac{\phi^3}{(1-\phi)^2}, \quad (19)$$

where $\bar{r^2}$ is the spatial average of the squared grain radii in the surroundings. $\kappa_1 = \alpha < r >^2$ is a constant prefactor, while $\kappa' = r'^2 f(\phi)$ captures permeability variations in space and time ($< r >$ is the mean grain radius in the system and r' is the local deviation from it, such that $r = < r > r'$). In the original Kozeny-Carman relation, $\alpha = 1/45$ [67] is a geometrical prefactor for spheres. In our simulations, we vary α to directly control the order of magnitude of the permeability between different simulations, independent of the grain size. This approach was suggested by [50–53, 56] and allows to overcome the numerical limitations on the usage of small numerical grains, with realistic radii, representative of experiments or field conditions. Varying α allows us to combine numerically feasible grain sizes with permeability values that represent natural systems. We stress that permeability changes due to skeleton deformation are accurately resolved through changes in the porosity. Appendix A presents numerical relations between grain size, time step, and permeability and discusses the validity of the grain size-permeability decoupling.

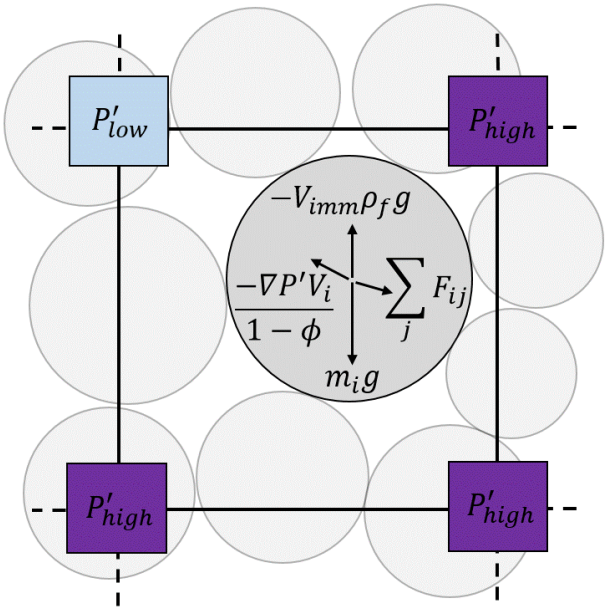

FIG. 1. Schematic representation of the forces in the model. Dynamic pore pressure gradients exert forces on each grain ($-(\boldsymbol{\nabla} P' V_i)/(1-\phi)$). These forces are inferred based on an interpolation scheme that interpolates the pressure gradients from grid nodes to the individual grains. As stated in Eq. (17), this force is added to gravity ($m_i \boldsymbol{g}$), buoyancy ($-V_{\mathrm{imm},i}\rho_f \boldsymbol{g}$) and the sum of contact forces ($\Sigma_j \boldsymbol{F}_{ij}$).

B. The setup of the numerical simulations

The numerical system (Fig. 2) represents a thin Hele-Shaw cell of spherical grains with grain radii between $0.8 - 1.2$ cm drawn from a distribution with a mean of 1 cm and a standard deviation of 1 cm. The system horizontal dimension is $L = 0.8$ m, and its height is $h \approx 0.28$ m. We ran simulations under two distinct modes: The first mode is "Hydrostatic Pore Pressure" (HPP) in which the fluid exerts a buoyancy force due to the constant hydrostatic pressure gradient on the grains ($-\rho_f g$), regardless of the grain dynamics. In this mode, we do not solve the fluid Eq. (13) and the last term of Eq. (17) is omitted, i.e., we neglect the dynamic forces

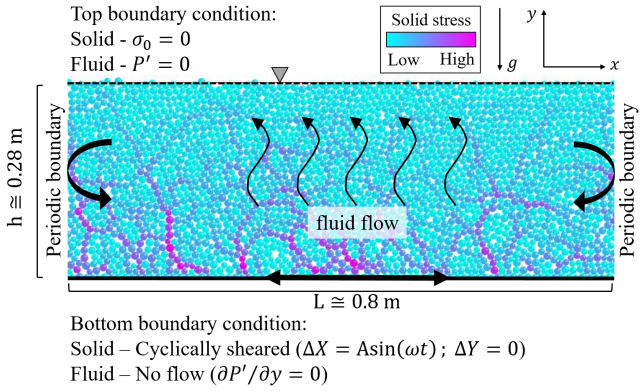

FIG. 2. Numerical system setup. The domain represents a Hele-Shaw cell. The bottom wall is constructed of half grains, glued together. At the top, there is no wall and the grains are free to move. The grains color-code corresponds to their relative solid normal stress. The dashed line marked by a triangle denotes the fluid level. In "Hydrostatic Pore Pressure" (HPP) simulations, the fluid exerts only buoyancy on the grains. In "Dynamic Pore Pressure" (DPP) simulations, deviations from hydrostatic conditions develop. The bottom wall is a no flow boundary and the upper fluid interface is a zero pressure boundary, allowing the fluid to drain. In the horizontal direction (x), the system is periodic. The dynamics is induced by cyclic shearing (horizontal shaking) of the bottom solid wall at a preset amplitude (A) and frequency (ω). Vertical displacement of the bottom wall is not allowed.

between the fluid and solid. The second mode is "Dynamic Pore Pressure" (DPP) in which the fluid and the grains are fully coupled. The local compaction/dilatation affects the fluid pressure and the local dynamic fluid pressure gradients exert forces on the grains in addition to the constant buoyancy force.

The bottom wall is constructed of half grains (drawn from the same distribution as the internal grains) glued together and a sinusoidal cyclic shear (horizontal shaking) is imposed on it, $X = A\sin(\omega t)$, where X is the bottom wall horizontal displacement, A is the amplitude, and $\omega = 2\pi f$ is the angular frequency ($f = T^{-1}$ is the temporal frequency and T is the periodicity). Vertical displacement of the bottom wall is not allowed. At the top boundary, there are no normal nor shear stresses on the solid phase. For the fluid phase, the bottom wall imposes a no flow boundary condition ($\partial P'/\partial y = 0$) and the top is a constant pressure boundary ($P' = 0$). The water level is set to be approximately equal to the height of the top grains in the initial configuration, and due to mass conservation, it does not change during the simulations. For both phases, the horizontal direction is periodic, allowing us to simulate a laterally extensive and unconfined layer. The dynamics are limited to a 2D space but the porosity in the simulations is calculated as a 3D porosity, assuming a monolayer of spheres occupying a cell of one mean grain diameter in width.

All of our simulations start with the same initial configuration, characterized by a porosity of $\phi_0 = 0.434$, which is denser than a 3D random loose packing. This initial configuration is generated by sedimenting grains on top of the bottom wall, shaking it for 0.53 seconds at a low normalized acceleration of $\Gamma = A\omega^2/g = 0.042$ ($g = 9.81$ m s^{-2}), and allowing complete relaxation. Each simulation is characterized by a single shaking frequency (ω), and by a single small horizontal displacement amplitude of $A = 0.0431$ cm or $A = 0.431$ cm, corresponding to 4.31% or 43.1% of the mean grain diameter. Different combinations of frequency and amplitude provide a range of normalized accelerations of $\Gamma = 0.06-0.3$.

The DPP simulations target drained conditions, characterized by De $\ll 1$. To achieve that, we modify α in Eq. (19) and choose relatively high permeabilities, though still within the natural range for soils (κ_0 ranges between $3.1 \cdot 10^{-12}$ and $6.1 \cdot 10^{-11}$ m^2). With $\eta = 10^{-3}$ Pa·s as the water dynamic viscosity and $t_0 = T$ (single shaking period), De ranges between $O(10^{-4})$ to $O(10^{-2})$, which means that our simulations indeed represent well-drained systems. Table I summarizes the parameter values used in the model.

TABLE I. Physical values used in the model

Grain density	$\rho_s = 2640$ kg m^{-3}
Grain Young's modulus	$E = 10^{10}$ Pa
Grain mean radius	$r_s = 0.5$ cm
Grain friction coefficient	$\mu = 0.5$
Grain normal stiffness	$k_n = 10^8$ N m^{-1}
Grain tangential stiffness	$k_s = 2.64 \cdot 10^8$ N m^{-1}
Grain damping coefficient	$\gamma = 2.16 \cdot 10^5$ s^{-1}
Fluid density	$\rho_f = 1000$ kg m^{-3}
Fluid compressibilty	$\beta = 4.5 \cdot 10^{-10}$ Pa^{-1}
Fluid dynamic viscosity	$\eta = 10^{-3}$ Pa s
Gravitational acceleration	$g = 9.81$ m s^{-2}

IV. RESULTS

Figure 3 depicts trends of grain layer compaction in our simulations. The compaction is presented as the deviation of the average porosity from its initial value, $\Delta\langle\phi\rangle = \langle\phi(t)\rangle - \phi_0$, normalized by the initial value, ϕ_0. The observed compaction trends may be categorized into two representative end-members divided by $\Gamma_c \simeq 0.15$: At low accelerations ($\Gamma < \Gamma_c$, red and blue curves in Fig. 3), both simulation setups of Hydrostatic Pore Pressure (HPP, Fig. 3 (a)) and Dynamic Pore Pressure (DPP, Fig. 3 (b)) show no significant compaction. At $\Gamma \geq \Gamma_c$ (black, grey, pink and green curves in Fig. 3) both HPP and DPP simulations show significant compaction, where the porosity decreases by more than $\sim 1\%$ with respect to its initial value.

The dynamics of the compaction (that occurs for $\Gamma \geq 0.15$), differs between the HPP and DPP cases: In HPP simulations, the rate of compaction decreases with time, and the compaction trend varies between the simulations.

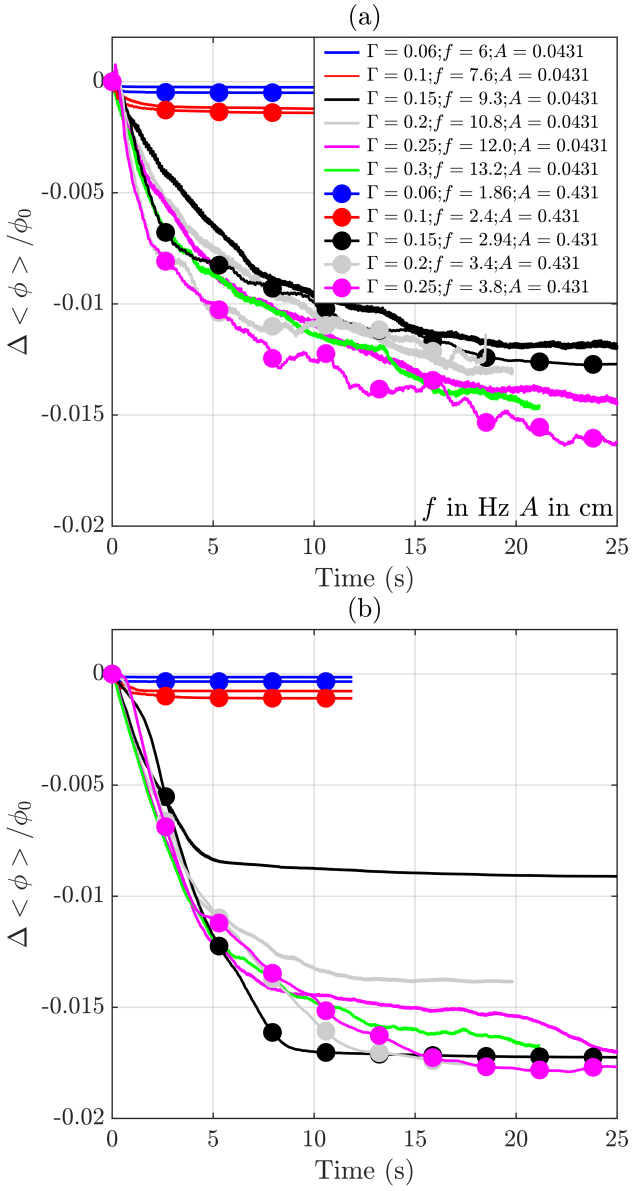

FIG. 3. Normalized average porosity change as a function of time. Two different shaking amplitudes (low amplitude $A = 0.0431$ cm, solid line, and high amplitude $A = 0.431$ cm, circles on lines) are compared for variable acceleration, Γ. (a) Hydrostatic pore pressure simulations (HPP). Compaction occurs only when acceleration exceeds a critical value, $\Gamma_c = 0.15$ (black, grey, pink and green curves). (b) Dynamic pore pressure simulations (DPP) with high permeability ($\kappa_0 = 6.1 \cdot 10^{-11}$ m^2, De $= 3 \cdot 10^{-3} - 4.6 \cdot 10^{-4}$). As in the HPP simulations, compaction occurs only when acceleration exceeds $\Gamma_c = 0.15$. High acceleration DPP simulations initially follow a single linear compaction trend. When Γ is close to Γ_c (black curves) compaction depends on the shaking amplitude.

In contrast, the initial compaction rate of the DPP simulations is constant and approximately the same across different runs, despite the different shear parameters. The linear trend continues for about 5 seconds, after which the rate of compaction gradually decreases. For $\Gamma \simeq \Gamma_c$, the DPP compaction trend is amplitude-dependent. For a low shaking amplitude (black solid curve in Fig. 3 (b)), both final compaction and transient time are lower. Importantly, all the simulations shown in Fig. 3 (b) were conducted with the same order of magnitude permeability. When permeability is changed, the compaction curves change dramatically, as we demonstrate next.

Figure 4 shows the compaction curves of high acceleration DPP simulations ($\Gamma = 0.2 - 0.25$), with amplitudes $A = 0.0431 - 0.431$ cm, and variable characteristic permeability $\kappa_0 = 3.1 \cdot 10^{-12} - 6.1 \cdot 10^{-11}$ m^2 that leads to variable De $= 0.00094 - 0.054$. Note that despite the order of magnitude change in the permeability, De remains $\ll 1$, which ensures that the system is well drained. The figure shows that for a given permeability (equal κ_0 are marked with the same markers in Fig. 4), the compaction curves collapse and show a similar linear rate of compaction, regardless of acceleration, frequency and shearing amplitude. Furthermore, a positive correlation is observed between the permeability and the compaction rate during the initial phase of compaction, whereby in simulations with a lower permeability, the layer compacts slower and consequently for a longer duration.

In order to explore differences in both the solid and the fluid variables, between compactive behavior that occurs under high cyclic accelerations, and non-compactive behavior under low accelerations (as seen in Fig. 3), Figures 5 and 6 explore representative simulations with low and high accelerations in DPP and HPP cases. The low acceleration simulation ($\Gamma = 0.1 < \Gamma_c$) exhibits rigid body translation, with almost no internal strain. More specifically, Fig. 5 (a), (b) and inset shows that the horizontal grain velocity is independent of depth, i.e., $\partial u_{sx}/\partial y = 0$, for both HPP and DPP. In contrast, for high acceleration ($\Gamma = 0.25 > \Gamma_c$), in both the HPP and DPP simulations the dynamics is radically different. In the HPP simulation, Fig. 6 (a) and inset show a clear delay between the bottom wall velocity, where the strain is imposed, and the layers above it. This reflects the fact that the shear velocity imposed on the bottom wall is transmitted upward via a shear wave. In contrast, the DPP response to the same high acceleration ($\Gamma = 0.25$) (Fig. 6 (b)) includes the formation of a zone with nearly zero horizontal grain velocity ($u_{sx}(y,t) \simeq 0$, orange zone bordered by a black line in Fig. 6 (b)). When this zone forms (after a few shearing cycles), it extends from near the bottom wall to the free surface. However, its thickness shrinks with time, until it disappears completely. In the case depicted in Fig. 6 (b), this occurs after 5 seconds. A zone with zero horizontal velocity means that the horizontal shear strain imposed at the bottom wall does not propagate through this horizontal transiently stagnant layer. After this episode, the DPP simulation behaves similarly

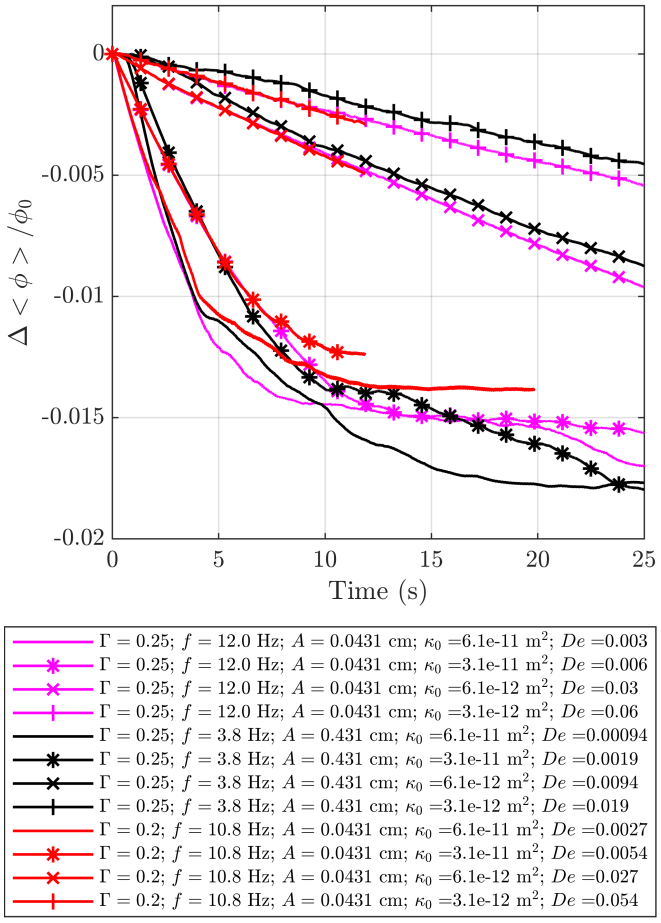

FIG. 4. Normalized average porosity change as a function of time for high acceleration, dynamic pore pressure (DPP) simulations with variable permeability. Simulations of equal characteristic permeability (κ_0, depicted by the same symbol) have roughly the same compaction rate during the initial rapid linear compaction phase, regardless of the acceleration (Γ), frequency (f) and amplitude (A). All the simulations are well-drained (De $\ll 1$).

to the HPP simulation, with propagating shear waves from the base to the top. The episode of nearly zero horizontal grain velocity correlates temporally and spatially with rapid downward vertical solid grain velocity (u_{sy}) as depicted in Fig. 6 (d) by an orange zone bordered by a black line.

To clarify the micro-mechanics related to this behavior, Fig. 7 presents snapshots of the grain dynamics during a DPP high acceleration simulation ($\Gamma = 0.25$). Immediately after the imposed shaking starts (Fig. 7 (b)) the grain skeleton is solid (the stress chains transmit large stresses, as indicted by their purple color) and horizontal shear deformation is transmitted from the bottom wall via transient granular vortexes (as indicated by the black arrows in Fig. 7 (c)). After a few cycles (Fig. 7 (d)), the stress chains almost vanish and shear is not transmitted upward. The thickness of the sheared layer gradually increases (Fig. 7 (e)) until the whole layer regains its strength and is sheared as in the very beginning (Fig. 7 (f)).

To identify the role that fluid pressure plays in this behavior, we follow the spatial and temporal evolution of the dynamic pore pressure gradient ($\boldsymbol{\nabla} P'$, where P' is the pressure deviation from hydrostatic) in the DPP simulations. Figure 8 depicts its vertical component, averaged horizontally and normalized by the static effective vertical stress gradient ($\boldsymbol{\nabla} P'_y / \boldsymbol{\nabla} \sigma_0$). For the low acceleration simulation ($\Gamma = 0.1$), with the exception of the few first cycles, $\boldsymbol{\nabla} P'_y$ is close to zero (Fig. 8 (a)). When the acceleration is high ($\Gamma = 0.25 > \Gamma_c$), the gradients of the dynamic pore pressure rise until they become comparable to the static effective vertical stress ($\boldsymbol{\nabla} P'_y / \boldsymbol{\nabla} \sigma_0 \approx 1$, white zone bordered by a black line). This high pressure gradient zone progressively shrinks with time until it disappears. In the simulation presented in Fig. 8, the zone disappears after about five seconds from the onset of shaking. This transient zone of high pressure gradient correlates spatially and temporally with the high vertical grain velocity episode observed in Fig. 6 (d) and with the zero horizontal grain velocity depicted in Fig. 6 (b). Outside of this zone, the mean value of $\boldsymbol{\nabla} P'_y$ decreases towards zero, although the instantaneous values are fluctuating and episodically may reach $\boldsymbol{\nabla} P'_y / \boldsymbol{\nabla} \sigma_0 \approx 1$. The same behavior is observed in Fig. 9, where the dynamic pore pressure (P') is plotted vs. time at three different depths in the layer. Upon shaking initiation, the pressure at each depth (solid curves) rises towards the static normal effective solid stress value (dashed lines), and then it decreases back to zero. The closer the point is to the surface, the longer is the duration of the elevated pore pressure. This observed trend in pore fluid pressure evolution is in an excellent agreement with the numerical study of [8].

V. DISCUSSION

Three important outcomes arise from our theoretical analysis and simulation results. The outcomes apply specifically to the dynamics of a saturated grain layer that is cyclically sheared in the horizontal direction, when fluid can freely drain from the layer during the time scale set by the shearing periodicity, i.e., where De $\ll 1$.

First, we find an acceleration-controlled transition at $\Gamma_c \approx 0.15$, between a non-compactive and compactive behaviors, in both HPP and in DPP simulations. A similar acceleration-dependent threshold that separates rigid from liquid-like behavior was observed previously by Clément et al. [66] in DEM simulations, using a different code that implements only HPP conditions. They identified a threshold that corresponds to $\Gamma_c = \mu_a(\rho_s - \rho_f)/\rho_s$, where μ_a is the macroscopic apparent friction coefficient, above which grains slide past each other, and initiate grain re-arrangement. In DEM simulations, μ_a is smaller than the assigned surface grain friction, and in our case

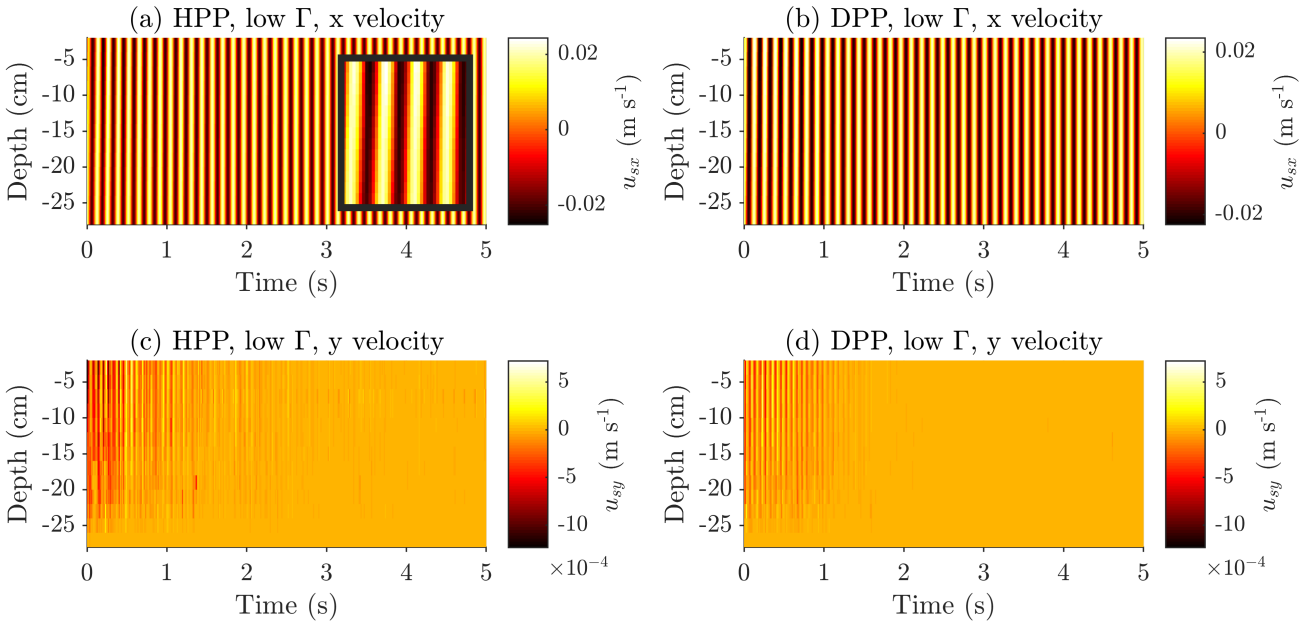

FIG. 5. Horizontally averaged solid grain velocity as function of depth (y) and time (t) for a low acceleration simulations ($\Gamma = 0.1, A = 0.0431$ cm). The bottom wall is at $y = -28$ cm where the horizontal displacement is imposed, and $y = 0$ cm is the free surface. The top panels show the horizontal grain velocity (u_{sx}) in a hydrostatic pore pressure (HPP) simulation (a) and a dynamic pore pressure (DPP) simulation (b). The grain layers move as a rigid body following the imposed velocity at the bottom, as shown by the inset in (a) that focuses on several cycles. The bottom panels show the vertical velocity (u_{sy}) in the hydrostatic pore pressure (HPP) (c) and the dynamic pore pressure (DPP) (d) simulations. Minor fluctuations occur during the first second, and afterwards the grains are stagnant in the vertical direction (orange color).

$\mu = 0.5$ and $\mu_a \approx 0.25$ [68]. The acceleration threshold for compaction of grains arises from a force balance between friction (when the normal force is modified by buoyancy) and imposed inertia. Our simulations show that the same criterion and threshold are applicable also in DPP simulations, where dynamic pore pressure gradients develop. This occurs because at the beginning of a DPP simulation, before any dynamic pore pressure or fluid flow evolves, the system is similar to a HPP system, in which the pressure gradient drag force is neglected. Hence, the initiation of compaction by sliding obeys the same threshold acceleration predicted for a HPP setting. We note that close to the critical acceleration, the behavior can be more complex. Particularly, our simulations show that the shearing amplitude may control the specific dynamics when $\Gamma = \Gamma_c$ (see Fig. 3 (b) black curves).

The second important conclusion, is that fluid pressure evolution is controlled by, and coupled to, the compaction dynamics of grains. Compaction generates high pore pressure, high pressure gradients, and as an outcome, fluid outflow. At the same time, pressure gradients weaken (and even completely diminish) the solid contacts in between the grains, which facilitates grain rearrangement in the form of compaction. We find that despite the drained conditions, which are achieved since the layer can drain at the time scale of a single cycle of shaking ($De \ll 1$), pore pressure rises for a substantial duration to a value that is equal to the lithostatic stress. The physics of this pressure rise, and its coupling to compaction, is concluded from simulations, and also from the following theoretical analysis.

Assuming that significant pressure gradients develop only in the vertical direction, and applying the boundary condition of a vertical stationary and impermeable bottom boundary wall, Eq. (16) reduces to:

$$u_{sy} = \frac{\kappa_0}{\eta}\frac{\partial P'}{\partial y}. \tag{20}$$

This relation is depicted in Fig. 10 where the two sides of Eq. (20) are plotted for a high acceleration DPP simulation, normalized by their theoretical maximum values. A linear relation with a close-to-unity slope emerges even for the raw fluctuating data (Fig. 10 (a)). When the fluctuations are filtered (Fig. 10 (b)), an additional trend appears, where at the beginning of the simulation (blue markers), the values are close to their expected maximum, at the end of the simulation they are equal zero (yellow markers) and the transition between these extreme values is continuous in time. The agreement between the numerical results that are based on the full three-terms fluid equation (13) and the theoretical prediction, equation (20) that neglects the time-dependent term when De $\ll 1$, confirms that the non-dimensional

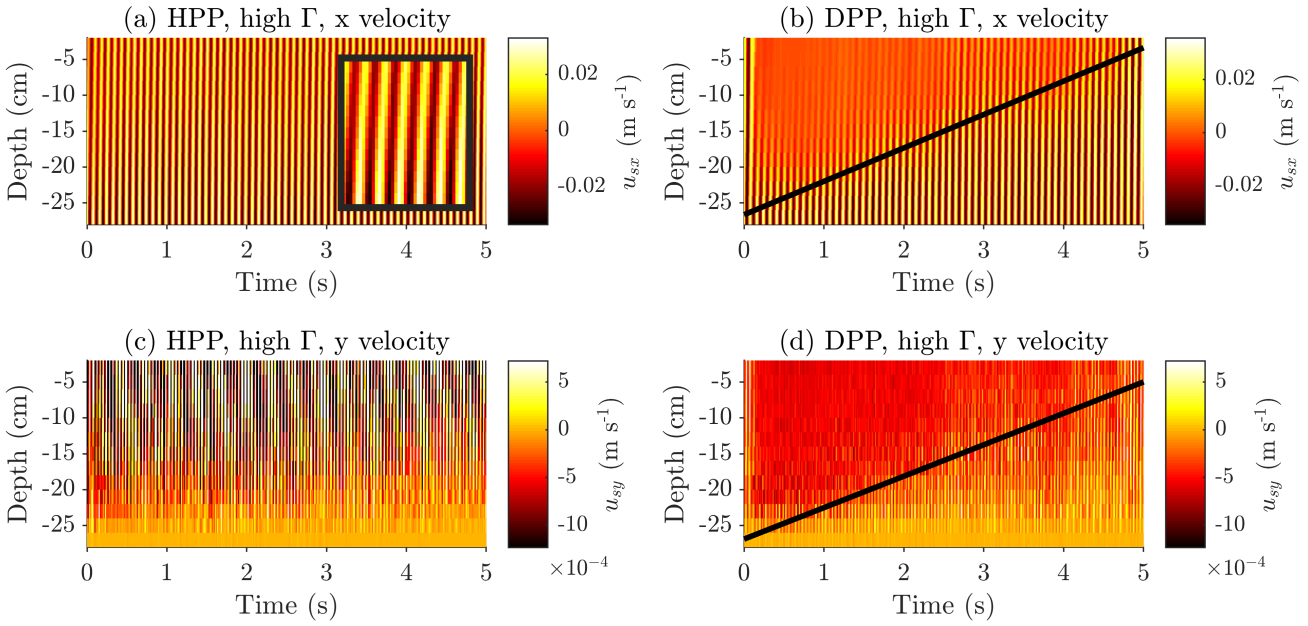

FIG. 6. Horizontally averaged solid grain velocity as function of depth (y) and time (t) for high acceleration simulations ($\Gamma = 0.25, A = 0.0431$ cm) under both HPP and DPP conditions. The top panels depict the horizontal velocity (u_{sx}). (a) In a hydrostatic pore pressure (HPP) simulation, internal strain is observed, where the shear is transmitted from the bottom wall upward, as shown by the inset that focuses on several cycles. (b) In a dynamic pore pressure (DPP) simulation, a similar internal strain is observed, yet it is limited to a lower zone, overlain by an upper stagnant domain of nearly zero horizontal velocity (orange). The bold black line marks the border between the straining, oscillating domain, and the stagnant domain, and its slope is approximated by Eq. (24). This line depicts an upward propagating front that swipes through the DPP system, separating two dynamical regimes. The bottom panels show the vertical velocity (u_{sy}). (c) In a hydrostatic pore pressure (HPP) simulation, we observe oscillatory change in velocity with positive and negative values (i.e., upward and downward, respectively) that continues throughout the simulation. (d) In a dynamic pore pressure (DPP) simulation, the same upward propagating front (bold line) is observed. The front separates a domain with sustained rapid downward velocity (dark red) from an underlying stagnant layer that is not compacting anymore.

Deborah number, De, controls the dominant coupled dynamics of the system. More specifically, for drained conditions, the dynamic pressure gradient is exactly proportional to the grain velocity.

With the specified bottom boundary conditions, the vertical solid grain velocity is directly related to the compaction rate (see Appendix B for a detailed derivation):

$$u_{sy} = \frac{\partial \langle \phi(y,t) \rangle}{\partial t} \frac{H}{(1-\phi_0)}, \tag{21}$$

where ϕ_0 is the initial porosity and $\frac{\partial \langle \phi(y,t) \rangle}{\partial t} = \frac{1}{H}\int_0^H \frac{\partial \phi(y,t)}{\partial t} dy$ is the depth averaged compaction rate over a sub-layer that extends from the bottom wall to height H above the bottom ($0 < H \leq \mid h \mid$).

Equations (20) and (21) reveal that the source for elevated pore pressure in a drained layer is the vertical velocity of the solid grains, which is proportional to the rate of compaction. The vertical velocity in turn, is set by a volume conservation consideration, which requires that grain compaction rate must be balanced by the rate of fluid expulsion. The expulsion rate is controlled by the fluid viscosity, the layer permeability, and the evolving pressure gradients. More specifically, when the system compacts, the pore pressure rises, with gradients exceeding hydrostatic values. When the lithostatic limit for pressure gradient, $\nabla P'_y = \nabla \sigma_0$, is reached, the solid stresses completely vanish and the net force on the grains is zero. At this point, the grains will maintain a constant downward velocity of

$$u_{sy} \approx (\kappa_0/\eta)\nabla\sigma_0. \tag{22}$$

This steady-state compaction and pressurization phase ends when the porosity reaches some lower critical value. In our simulations, we find that this critical value corresponds to $\phi_c = 0.429 \pm (9.5 \cdot 10^{-4})$ which is higher than the reported 3D random close packing of spheres $\phi^{3D}_{RCP} = 0.36 \pm 0.02$ [69]. This higher value probably reflects our choice to measure the porosity as a 3D property over a mono-layer of spheres. The abrupt reduction in compaction rate once a lower critical porosity is reached, agrees with [38], who studied vertical shaking.

Equation (20) also indicates that at any point in time, the pore pressure gradient is independent of the former porosity and state of pressure, and instead is sen-

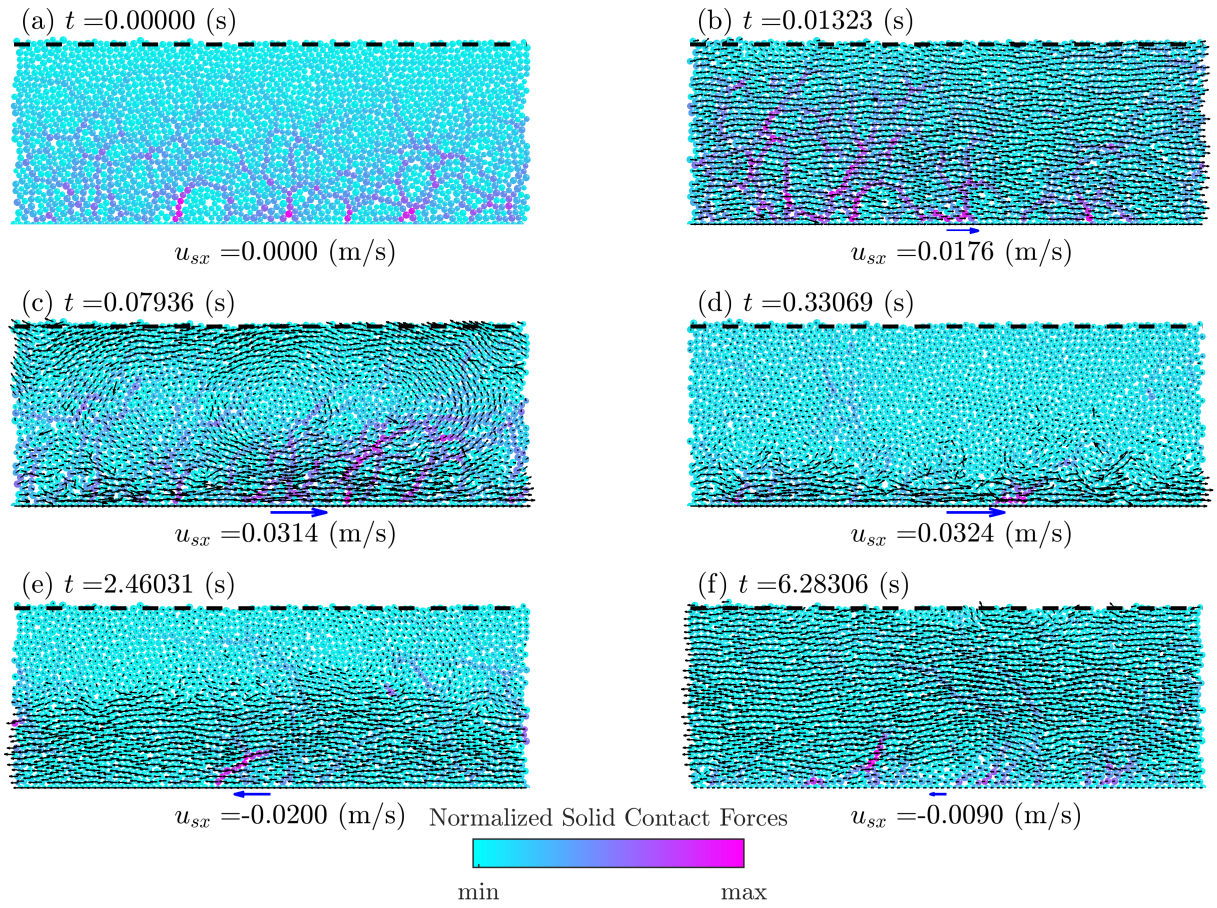

FIG. 7. Snapshots of granular dynamics during a high acceleration simulation ($\Gamma = 0.25$) with dynamic pore pressure (DPP). The colors of the grains indicate their relative solid normal contact force (normalized to the maximum normal force in each frame, (a) 3.5 N (b) 0.7 N (c) 7.5 N (d) 1.7 N (e) 2.6 N and (f) 1.0 N). The black arrows depict the solid grain velocity. The blue arrow at the base indicates the imposed bottom wall velocity, exaggerated by a factor of 5 with respect to the black arrows. The dashed black line shows the position of the fluid top surface. (a) Before the initiation of shear, the layer is at rest. (b) When the imposed shaking starts, the grain skeleton behaves in a solid manner, with percolating stress chains capable of transmitting the shear waves from the bottom wall. (c) Some of the motion occurs via transient granular vortexes. (d) After a few cycles, the stress chains almost vanish and shear is not transmitted through the upper parts of the layer. (e) The thickness of the bottom sheared zone gradually increases. (f) The whole layer is sheared as in the very beginning. See also a movie in the supplementary material [URL will be inserted by publisher].

sitive only to the instantaneous rate of skeleton compaction/dilation. At the same time, equations (20) - (22) reveal that the rate of compaction is controlled by the permeability and is independent of the imposed shear parameters. The higher the permeability of the layer, the faster the grains compact.

These insights about the dependency between the rate of compaction, the pressure gradient, and the permeability for a fully drained system, when De $\ll 1$, are well demonstrated in our simulation results. Specifically, a clear distinction can be made between HPP and DPP simulations. In HPP simulations with high accelerations, the grains remain in contact with each other during the whole simulation, as witnessed by their ability to transmit the shear waves from the bottom wall (Fig. 6 (a) and (c)). In contrast, in DPP simulations of high accelerations, after a few shaking cycles, the dynamic pore pressure gradient becomes equal to the static effective stress gradient ($|\nabla P'_y/\nabla\sigma_0| \approx 1$, Fig. 8 (b)). The solid grain velocity is then maximal and proportional to the dynamic pore pressure gradient and to the permeability, as shown in Fig. 4. At this stage, the fluid pressure is equal to the lithostatic stress within the compacting zone which means that the fluid (and not the grains) carries the load, solid stress chains vanish, and shear waves are not transmitted (see Fig. 6 (b) and Fig. 7 (d)).

The last important finding of this work is the identification of an upward moving front, that separates an upper pressurized compacting region from a lower, fully compacted zone. This front arises because the downwards

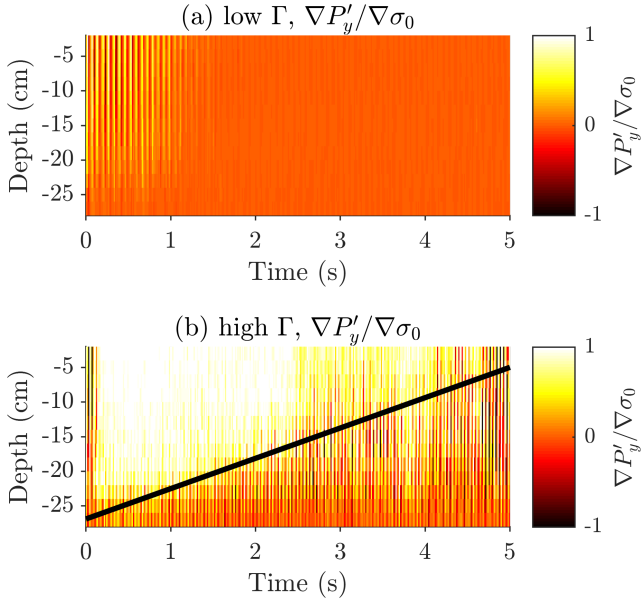

FIG. 8. Dynamic vertical pore pressure gradient ($\nabla P'_y$) normalized by the gradient of the effective static normal stress ($\nabla\sigma_0$) for a low amplitude simulations ($A = 0.0431$ cm). This ratio is expected to be unity when $\nabla P'_y = \nabla\sigma_0$ (white), zero in the hydrostatic case (orange) and negative when the pressure is below hydrostatic value (dark red). (a) At low acceleration ($\Gamma = 0.1$), after some initial fluctuations, the pore pressure gradients vanish. (b) at high acceleration ($\Gamma = 0.25$), a domain where $\nabla P'_y = \nabla\sigma_0$ develops after several cycles. The thickness of this domain decreases with time (white region). The domain is bordered by a bold black line whose slope is given by Eq. (24). This line represents an upward moving front, separating a high pressure-gradient zone from a zone of hydrostatic pressure gradient on average. The high pressure gradient zone is temporally and spatially correlated with the high vertical velocity zone of Fig. 6 (d) and with the vanishingly small horizontal velocity zone in Fig. 6 (b).

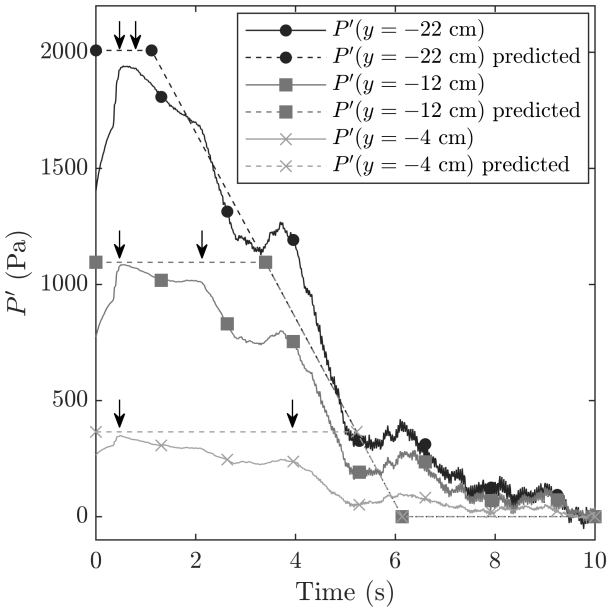

FIG. 9. Dynamic pore pressure (P') vs. time during a high acceleration simulation ($\Gamma = 0.25$ and $A = 0.0431$ cm) at three depths in the layer. The data is smoothed over a window of eight cycles. The dynamic pressure increases after a few cycles towards the effective static normal stress (depicted by the horizontal portions of the dashed lines) and than gradually decreases to zero. This high pressure episode, whose approximated start and end points are depicted by black arrows, is sustained longer at shallower depths, as predicted by the compaction front model (Eqs. (20) and (24), dashed lines).

grain movement is restricted by the vertical stationarity of the bottom wall, which means that once grains near the bottom reach a higher packing density, the rate of compaction decreases. Since compaction is the driver for pressurization, when compaction stops, the pressure gradient in this fully-compacted layer drops to a hydrostatic value. The pressurized layer is thus restricted to an upper layer, above the fully compacted region and its thickness reduces over time. The rate at which the pressurized layer thickness decreases is dictated by the velocity of the "compaction front" that transmits upward the information about the stationary bottom wall. To find this velocity, we express the compaction front as a discontinuity and write the grain's mass conservation over the front, in the front's frame of reference:

$$\rho_s(1-\phi_0)(u^0_{s,y}-u_{front}) = \rho_s(1-\phi_c)(u^c_{s,y}-u_{front}), \quad (23)$$

where u_{front} is the front's velocity, ϕ_0 and $u^0_{s,y}$ are the porosity and grain velocity before the front arrives, respectively, and ϕ_c and $u^c_{s,y}$ are the porosity and grain velocity after the front arrives, respectively. Since $u^c_{s,y} \approx 0$ the velocity of the front is:

$$u_{front} = \frac{\phi_0 - 1}{\phi_0 - \phi_c} u^0_{s,y}. \quad (24)$$

Evaluating u_{front} in Eq. (24) with $u^0_{s,y} = (\kappa_0/\eta)\nabla\sigma_0 = (\kappa_0/\eta)(1-\phi_0)(\rho_s - \rho_f)g$ as the solid vertical velocity during the full pressurization stage (Eq. (22)), leads to:

$$u_{front} = \frac{\phi_0 - 1}{\phi_0 - \phi_c} \frac{\kappa_0}{\eta} \nabla\sigma_0, \quad (25)$$

which provides a good prediction for the front velocity in our simulations. The front velocity dictates the slope of the bottom boundary of the nearly zero horizontal grain velocity domain in Fig. 6 (b), the maximum vertical grain velocity domain in Fig. 6 (d) and the pressurized domain in Fig. 8 (b) (all marked with a black line). The compaction front model, expressed by Eqs. (24), (25) and (20), predicts the dynamic pressure profiles in the layer over time. We express the front position as:

$$y_{front} = y_0 + u_{front} \cdot t, \quad (26)$$

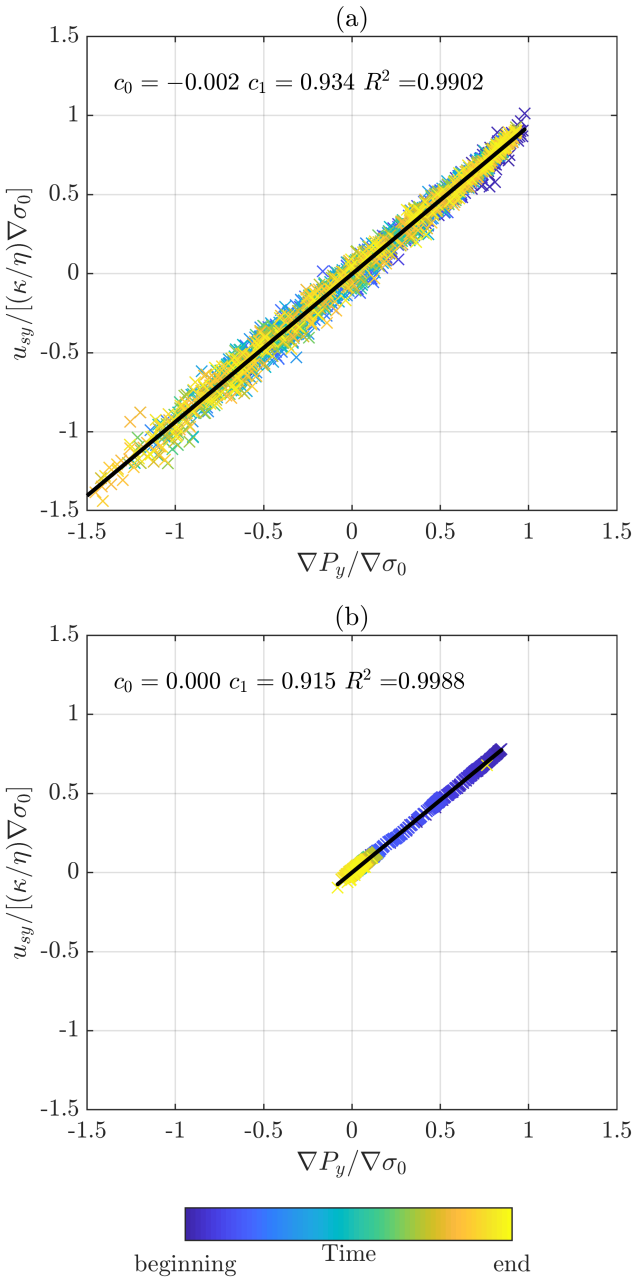

FIG. 10. Average vertical velocity of the solid grains, normalized by $(\kappa_0/\eta)\nabla\sigma_0$, vs. vertical gradients of average dynamic pore pressure (normalized by $\nabla\sigma_0$) from high acceleration, DPP simulation ($\Gamma = 0.25$; $A = 0.0431$ cm). The markers color represents time in the simulation: blue is the beginning of the simulation and yellow is the end. The data shows that in well-drained systems, Eq. (20) captures the coupled grain compaction and fluid pressurization dynamics, both for the instantaneous response as seen in the original data, panel (a), and when the data is smoothed over a window of eight cycles, panel (b). The numerical data fits well a line with a slope of one (black line, c_0 is the intersection and c_1 the slope).

where y_0 is negative and indicates the depth at which the front first appears, and $y_{front} = 0$ means that the front has propagated all the way to the surface. With this definition, the pressure profile is made of two linear segments:

$$P'(y,t) = \begin{cases} \sigma_0(y) & \text{for } y \geq y_{front} \\ \sigma_0(y_{front}) & \text{for } y < y_{front} \end{cases} \tag{27}$$

This means that at the upper part of the layer, before the front passes ($y > y_{front}$), the slope of the pressure profile is expected to be equal to the slope of the effective static normal stress. At the lower part of the layer, after the front has passed ($y < y_{front}$), we expect a zero slope, i.e. constant pressure with depth. The predicted profiles at different times during the simulation (Eqs. (26) and (27)) are presented in Fig. 11 as dashed lines, and compared to the numerical profiles (solid lines). The predicted and observed profiles overall agree, and deviations may arise from (1) the finite thickness of the compaction front, that is not accounted for in the theory of equation (24), (2) the bottom sub-layer instantaneous compaction/dilatation around an average vertical stationarity, and (3) the instantaneous grain velocity oscillations around the predicted compaction velocity. The overall physical picture of the compaction front with the distinct zones that it forms is summarized in Fig. 12.

As an implication, one can attempt to compare our modeling predictions to observations in earthquakes. Our simulated layer models a fully saturated soil layer that is shaken by seismic waves. An upward propagating compaction front is predicted. Within the pressurized compacting sub-layer, before the arrival of the compaction front, contact stresses between grains vanish and shear waves cannot be transmitted. We predict that this sub-layer, which exhibits the properties of liquefaction [7], will become thinner with time, and progressively confined to the shallower depths. This prediction is supported by field observation from Holzer et al [70], who measured fluid pressure directly in the ground, during an earthquake. They find that high pore pressure and liquefaction decay from the bottom upward. Our results have another important implication for soil liquefaction that relates to the drainage conditions. Most commonly, liquefaction is assumed to initiate under undrained conditions [40, 71], since it is believed that fluid flow relaxes the pore pressure. Our simulations and theory show that liquefaction can initiate under well-drained conditions, in support of recent experiments [39]. This has critical implications for geophysical earthquake hazard assessment.

VI. SUMMARY

In the current work, we explore theoretically and numerically the coupled grain - interstitial pore fluid dynamics of a saturated granular layer, subject to low overburden stresses and to cyclic horizontal displacements.

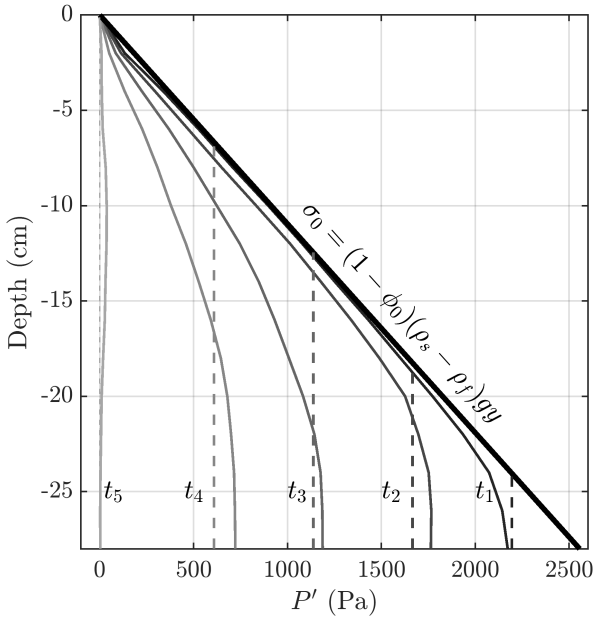

FIG. 11. Profiles of dynamic pore pressure (P') at different times ($t_1 = 0.65$ s; $t_2 = 1.97$ s; $t_3 = 3.29$ s; $t_4 = 4.62$ s; $t_5 = 9.47$ s) during a high acceleration DPP simulation with $\Gamma = 0.25$ ($A = 0.0431$ cm). The bold line shows the effective static normal stress. The dashed curves depict the dynamic pore pressure profiles, as predicted by the compaction front model (Eqs. (24)-(27)). The thin solid curves are the numerically derived dynamic pore pressure profiles. The simulations and the model show good agreement. See text for sources of deviations.

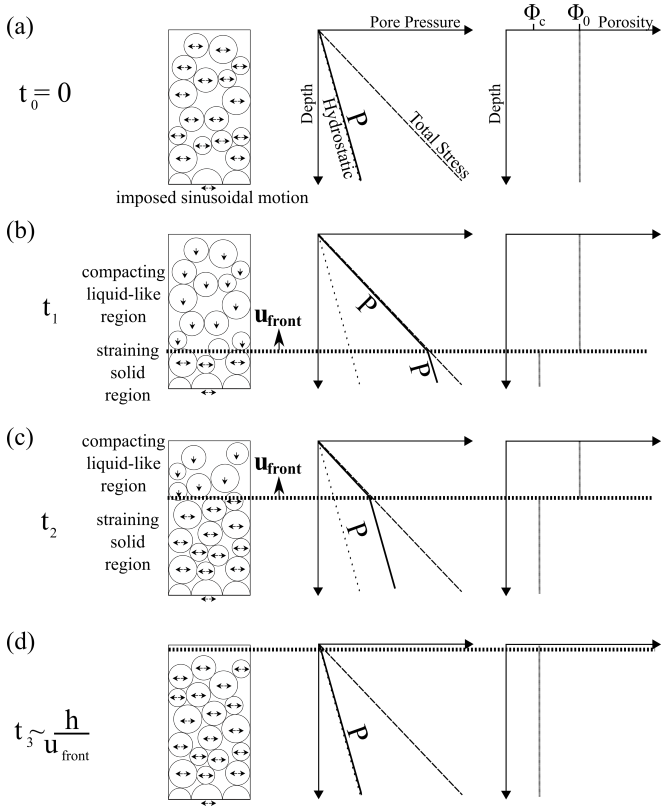

FIG. 12. Schematic cartoon that summarizes the evolution of the coupled grain-fluid dynamics. (a) Initially, the layer has a porosity ϕ_0 and the grains move horizontally with a velocity u_{sx}, imposed by the cyclic shear of the bottom wall. The pore pressure is hydrostatic. (b) After a few shaking cycles, the grain layer is divided into two sub-layers by a compaction front that moves upward at a rate u_{front}. The grains at the top sub-layer are settling at a velocity of u^0_{sy}, their horizontal velocity is vanishingly small, and the pore pressure is elevated to the value of the initial total stress. The bottom sub-layer has compacted to a porosity of ϕ_c, the grains move following the cyclical horizontal shear and the pressure gradient is hydrostatic, although the pressure itself is elevated and set by the value of the pressure at the compaction front. (c) At a later time, The compaction front has progressed upward and with it, the depth at which the pressure gradient becomes hydrostatic. (d) After some time (which depends on the compaction front velocity and the layer height), the compaction front has already passed, and the whole layer has a ϕ_c porosity. The whole layer follows the imposed cyclic shear at the bottom.

Targeting specifically a setting representative of an upper soil layer responding to an earthquake seismic excitation, our study focuses on the layer compaction, pore fluid pressurization and fluid flow under well-drained conditions, whereby the pore fluid can flow out of the grain layer during the shaking period. A non-dimensional analysis reveals that the drainage conditions is a function of the non-dimensional De number, which, in the current setting, is the ratio between the time scale of pore pressure diffusion and the shaking periodicity. It was previously thought that when fluid can easily flow out of the system (De $\ll 1$ conditions), fluid pressure does not rise significantly and does not play a significant role in the dynamics of the system. By contrast, this work shows analytically and numerically that even when De $\ll 1$, fluid pressure rises dramatically and the dynamics of the grains is significantly altered.

We identify two end-member behaviors, with a transition controlled by the shaking acceleration. At low accelerations, below a critical value, the system behaves rigidly, compaction is negligible and fluid pressure remains hydrostatic. At high accelerations, albeit still at a fraction of the gravitational acceleration, significant compaction occurs, coupled to high fluid-pressure gradients that support the grains. Here, the compaction is initially rapid and linear in time, and we find that the compaction rate is governed by the rate of fluid drainage, which in itself is a function of the layer permeability and the fluid viscosity. This constant compaction rate is independent of the shaking forcing. The duration and location of the pressurization event is well described as a compaction front (Fig. 12), that propagates up from the base of the layer. Before the arrival of the front, the interstitial fluid is over-pressurized to the level of the effective static normal stress, it flows upward fully supporting

the grains weight, which allows the grains to compact at a constant rate. After the front passage, grains are compacted and the fluid pressure gradient is hydrostatic. The good agreement between the numerical simulations and the compaction front model suggests that our theory can serve as a predictive tool to evaluate pressurization episodes in compacting, well-drained, grain-fluid systems.

Specifically, our results indicate that compaction, fluid flow, and pressurization are interdependent in horizontally shaken granular layers under drained conditions, with potential implications for earthquake-induced soil-liquefaction.

VII. ACKNOWLEDGEMENTS

SBZ acknowledges the support of INSTITUT FRANÇAIS D'ISRAËL and Campus France for Chateaubriand Fellowship, and University of Strasbourg. SBZ and EA thank the support of ISF grant #197/17. SP acknowledges Grant No. 19-21114Y by the Czech Science Foundation. RT acknowledges the support of the INSU ALEAS program, of the LIA France-Norway D-FFRACT, IPGS, and of the ITN FlowTrans, a funding from the European Union's Seventh Framework Programme for research under grant agreement no 316889. We thank KJ Måløy, YH Hatzor, V Vidal, JC Géminard, EG Flekkøy, E Altshuler, A Batista-Leyra and G Sanchez-Colina for interesting discussions.

Appendix A: Parameter scaling in the coupled grain-fluid model

The time step of the numerical solver was chosen to be small enough to resolve a single undissipated elastic collision between two grains, which lasts for $t_{col} = \sqrt{m/k_n}$, where m is average grain mass and k_n is grain normal stiffness (i.e., the spring constant used to compute the normal forces between grains in contact, using a linear displacement/force interaction model). We choose the time step to be $\Delta t = 0.1 \cdot t_{col}^{min}$, where t_{col}^{min} is the collision time associated with the smallest grain in our system. Using our model parameters, this restriction yields $\Delta t \approx O(10^{-7})$ s. The periodicity of the imposed horizontal shaking in our simulations is within the range of $T \approx O(10^{-2}) - O(10^{-1})$ s. This means that the simulation time step is sufficiently small to fully resolve this external forcing.

The dependency between the time step and grain size means that natural grain sizes could not be modeled in a reasonable simulation time. To overcome this limitation, we model grains that are larger than those found in nature. Since we are interested in the dynamics that occur within the natural range of permeabilities, we must decouple the permeability value from the modeled grain size. We do so by modeling the permeability as, $\kappa = \kappa_1 \kappa'(x, y, t)$ (Eq. (19)), where $\kappa_1 = \alpha < r >^2$ is a constant in each simulation, and $\kappa' = r'^2\phi^3/(1-\phi)^2$ varies in space and time (through changes in ϕ, and to a lesser extent, changes in r'^2). Under the effect of a pore pressure field and intergranular contact forces, grains are set in relative motion, which induces deformation and changes the porosity field ϕ (and possibly r'^2). We assume that this changes κ', without perturbing κ_1. By varying α in Eq. (19) we directly control the order of magnitude of the permeability between different simulations, independent of the grain size. This decoupling approach was proposed and successfully compared to experiments in [50–53, 56]. The "decoupled model" correctly captures the relevant dynamics because grain size does not dominate the physics. Instead, changes in the porosity and the order of magnitude of the permeability control the system behavior (Eqs. (21) and (22)). The excellent agreement between theory and simulations further shows that grain size does not affect the pore pressure evolution and the compaction rate, as predicted in Eqs. (22)-(26) and shown in Figures 9-11.

The small time step places a restriction on the permeability of the granular skeleton. To correctly resolve the fluid pressure diffusion equation (13) on the superimposed grid, we use the Courant–Friedrichs–Lewy condition $\Delta t < 0.5 \cdot \Delta x^2/D$. In our simulations, $\Delta x = 4 \cdot \bar{r}$, where $2 \cdot \bar{r}$ is the mean grain diameter, and $D = (\kappa_0)/(\beta\eta\phi)$ is the pore pressure diffusion coefficient. This restriction means that the permeability should be $\kappa < 10^{-10}$ m^2, and to ensure that, we set the α parameter in Eq. (19) to be $\alpha < 10^{-5}$.

Appendix B:

Reorganization of Eq. (3) shows that the divergence of the solid grain velocity can be related to the temporal and spatial change of porosity:

$$\nabla \cdot \boldsymbol{u_s} = \frac{1}{1-\phi}\left(\frac{\partial \phi}{\partial t} + \boldsymbol{u_s} \cdot \boldsymbol{\nabla \phi}\right). \tag{B1}$$

Since we do not expect large spatial gradients in porosity we neglect the last term of Eq. (B1) and by reducing it to the vertical dimension we get:

$$\frac{\partial u_{sy}(y,t)}{\partial y} \approx \frac{1}{1-\phi(y,t)} \frac{\partial \phi(y,t)}{\partial t}. \tag{B2}$$

Integration of Eq. (B2) from the bottom ($y = 0$) to an arbitrary height ($y = H$) gives:

$$\begin{aligned}
&\int_0^H \frac{\partial u_{sy}}{\partial y} dy = \\
&= \int_0^H \frac{1}{1-\phi(y,t)} \frac{\partial \phi(y,t)}{\partial t} dy \\
&= -\int_0^H \frac{\partial}{\partial t}[\ln(1-\phi(y,t))] dy \\
&= -\int_0^H \frac{\partial}{\partial t}[\ln(1-\phi_0-\delta\phi(y,t))] dy \\
&= -\int_0^H \frac{\partial}{\partial t}[\ln\Big((1-\phi_0)(1-\delta\phi(y,t)/(1-\phi_0))\Big)] dy \\
&= -\int_0^H \frac{\partial}{\partial t}[\ln(1-\phi_0) + ln(1-\delta\phi(y,t)/(1-\phi_0))] dy,
\end{aligned} \tag{B3}$$

where $\delta\phi$ is a small change from the initial porosity.

Since $\delta\phi(y,t)/(1-\phi_0) \ll 1$ we can expand a series $\ln\Big(1-\delta\phi(y,t)/(1-\phi_0)\Big) \approx -\delta\phi(y,t)/(1-\phi_0) - \delta\phi^2(y,t)/2(1-\phi_0)^2 + O(\delta\phi^3)$. Neglecting the high order terms of the expansion, Eq. (B3) becomes:

$$\begin{aligned}
&u_{sy}(H,t) - u_{sy}(0,t) \approx \\
&-\int_0^H \frac{\partial[\ln(1-\phi_0) - \delta\phi(y,t)/(1-\phi_0)]}{\partial t} dy \\
&= \frac{1}{1-\phi_0}\int_0^H \frac{[\delta\phi(y,t)]}{\partial t} dy \\
&= \frac{1}{1-\phi_0}\int_0^H \frac{\partial[\phi(y,t)-\phi_0]}{\partial t} dy \\
&= \frac{\partial\langle\phi(y,t)\rangle}{\partial t}\frac{H}{1-\phi_0},
\end{aligned} \tag{B4}$$

where $\frac{\partial\langle\phi(y,t)\rangle}{\partial t} = \frac{1}{H}\int_0^H \frac{\partial\phi(y,t)}{\partial t} dy$ is the spatial average compaction rate over a layer that extends from the bottom wall to height H. Applying the boundary condition of $u_{sy}(0,t) = 0$ to Eq. (B4):

$$u_{sy}(y,t) = \frac{\partial\langle\phi(y,t)\rangle}{\partial t}\frac{H}{1-\phi_0}, \tag{B5}$$

which correlates the solid grains flux over a surface to the change in porosity in a total medium volume.

[1] C. Marone, Laboratory-derived friction laws and their application to seismic faulting, Annual Review of Earth and Planetary Sciences **26**, 643 (1998).

[2] J. K. Morgan and M. S. Boettcher, Numerical simulations of granular shear zones using the distinct element method: 1. Shear zone kinematics and the micromechanics of localization, Journal of Geophysical Research **104**, 2703 (1999).

[3] K. Mair, K. M. Frye, and C. Marone, Influence of grain characteristics on the friction of granular shear zones, Journal of Geophysical Research **107**, 2219 (2002).

[4] P. A. Johnson and X. Jia, Nonlinear dynamics , granular media and dynamic earthquake triggering, Nature **437**, 871 (2005).

[5] K. Mair and S. Abe, 3D numerical simulations of fault gouge evolution during shear: Grain size reduction and strain localization, Earth and Planetary Science Letters **274**, 72 (2008).

[6] G. R. Martin, W. L. Finn, and H. B. Seed, Fundamentals of Liquefaction Under Cyclic Loading, Journal of the geotechnical engineering division **101**, 423 (1975).

[7] H. B. Seed, P. P. Martin, and J. Lysmer, Pore-water pressure changes during soil liquefaction, Journal of Geotechnical and Geoenvironmental Engineering **102**, 323 (1976).

[8] U. El Shamy and M. Zeghal, A micro-mechanical investigation of the dynamic response and liquefaction of saturated granular soils, Soil Dynamics and Earthquake Engineering **27**, 712 (2007).

[9] R. M. Iverson, The physics of debris flows, Reviews of Geophysics **35**, 245 (1997), arXiv:97RG00426 [doi:10.1029].

[10] D. Ertas and T. C. Halsey, Granular gravitational collapse and chute flow, Europhysics Letters **60**, 931 (2002), arXiv:0206046v1 [arXiv:cond-mat].

[11] O. Katz, J. K. Morgan, E. Aharonov, and B. Dugan, Controls on the size and geometry of landslides: insights from discrete element numerical simulations, Geomorphology **220**, 104 (2014).

[12] A. Lucas, A. Mangeney, and J. P. Ampuero, Frictional velocity-weakening in landslides on Earth and on other planetary bodies, Nature Communications **5**, 1 (2014).

[13] S. Parez and E. Aharonov, Long runout landslides : a solution from granular mechanics, Frontiers in Physics **3**, 80 (2015).

[14] S. Parez, E. Aharonov, and R. Toussaint, Unsteady granular flows down an inclined plane, Physical Review E **93**, 042902 (2016).

[15] H. J. Herrmann, J. Hovi, and S. Luding, *Physics of Dry Granular Media* (Springer Science & Business Media, 1997).

[16] E. Aharonov and D. Sparks, Rigidity phase transition in granular packings., Physical Review E **60**, 6890 (1999).

[17] E. Aharonov and D. Sparks, Shear profiles and localization in simulations of granular materials, Physical Review E **65**, 051302 (2002).

[18] E. Aharonov and D. Sparks, Stick-slip motion in simulated granular layers, Journal of Geophysical Research **109**, 1 (2004).

[19] P. Jop, Y. Forterre, and O. Pouliquen, LETTERS A constitutive law for dense granular flows, Nature **441**, 727 (2006).

[20] Y. Forterre and O. Pouliquen, Flows of Dense Granular Media, Annual Review of Fluid Mechanics **40**, 1 (2008).

[21] G. Sánchez-Colina, L. Alonso-Llanes, E. Martínez-Román, A. Batista-Leyva, C. Clement, C. Fliedner,

E. Altshuler, and R. Toussaint, Note: "Lock in accelerometry " to follow sink dynamics in shaken granular matter, Reviews of sceintific instruments **85**, 126101 (2014).

[22] L. Alonso-Llanes, G. Sanchez-Colina, E. Martínez, A. Batista-Leyva, R. Toussaint, and E. Altshuler, Intruder penetration in granular matter studied by Lock-in accelerometry, Revista Cubana de Fisica **33**, 95 (2016).

[23] S. A. Miller, A. Nur, and D. L. Olgaard, Earthquakes as a coupled shear stress-high pore pressure dynamical system, Geophysical Research Letters **23**, 197 (1996).

[24] L. Goren, E. Aharonov, D. W. Sparks, and R. Toussaint, Pore pressure evolution in deforming granular material: A general formulation and the infinitely stiff approximation, Journal of Geophysical Research: Solid Earth **115**, 1 (2010).

[25] R. M. Iverson and R. G. LaHusen, Dynamic pore-pressure fluctuations in rapidly shearing granular materials, Science **246**, 796 (1989).

[26] J. Desrues, R. Chambon, M. Mokni, and F. Mazerolle, Void ratio evolution inside shear bands in triaxial sand specimens studied by computed tomography, Geotechnique **46**, 529 (1996).

[27] M. Nicolas, P. Duru, and O. Pouliquen, Compaction of a granular material under cyclic shear, The European Physical Journal E **3**, 309 (2000).

[28] A. Skempton, The Pore-Pressure Coefficients A and B, Geotechnique **4**, 143 (1954).

[29] K. Terzaghi, *Theoretical Soil Mechanics* (John Wiley, New York, 1943).

[30] D. M. Hanes and D. L. Inman, Observations of rapidly flowing granular-fluid materials, Journal of Fluid Mechanics **150**, 357 (1985).

[31] J. Samuelson, D. Elsworth, and C. Marone, Shear-induced dilatancy of fluid-saturated faults : Experiment and theory, Journal of Geophysical Research **114**, 1 (2009).

[32] F. Boyer, E. Guazzelli, and O. Pouliquen, Unifying Suspension and Granular Rheology, Physical Review Letters **107**, 188301 (2011).

[33] L. Goren, E. Aharonov, D. Sparks, and R. Toussaint, The Mechanical Coupling of Fluid-Filled Granular Material Under Shear, Pure and Applied Geophysics **168**, 2289 (2011).

[34] D. R. Hewitt, J. S. Nijjer, M. G. Worster, and J. A. Neufeld, Flow-induced compaction of a deformable porous medium, Physical Review E **93**, 023116 (2016).

[35] G. Gauthier and P. Gondret, Compaction of liquid immersed granular packings by small upward flows, Physical Review Fluids **4**, 074308 (2019).

[36] C. Lesaffre, V. Mineau, D. Picart, and H. Van Damme, Densification under vibration of a saturated granular packing, Comptes Rendus de l'Académie des Sciences - Series IV - Physics **1**, 647 (2000).

[37] J. J. S. Jerome, N. Vandenberghe, and Y. Forterre, Unifying Impacts in Granular Matter from Quicksand to Cornstarch, Physical Review Letters **117**, 098003 (2016), arXiv:arXiv:1603.07013v1.

[38] S. Kiesgen de Richter, C. Hanotin, P. Marchal, S. Leclerc, F. Demeurie, and N. Louvet, Vibration-induced compaction of granular suspensions, European Physical Journal E **38**, 10.1140/epje/i2015-15074-7 (2015).

[39] O. Adamidis and G. Madabhushi, Experimental investigation of drainage during earthquake-induced Experimental investigation of drainage during earthquake-induced liquefaction, Geotechnique **68**, 655 (2018).

[40] A. Sawicki and J. Mierczynski, Developments in Modeling Liquefaction of Granular Soils, Caused by Cyclic Loads, Applied Mechanics Reviews **59**, 91 (2006).

[41] R. Snieder and A. van den Beukel, The liquefaction cycle and the role of drainage in liquefaction, Granular Matter **6**, 1 (2004).

[42] D. L. Lakeland, A. Rechenmacher, and R. Ghanem, Towards a complete model of soil liquefaction : the importance of fluid flow and grain motion, Proceedings of the royal society **470** (2014).

[43] B. M. Das, *Principles of soil dynamics* (PWS-KENT, Boston, 1993).

[44] S. L. Kramer, *Geotechnical earthquake engineering* (Prentice Hall, Inc., Upper Saddle River, New Jersey, 1996).

[45] K. Ishihara, Liquefaction and flow failure during earthquakes, Geotechnique **43**, 351 (1993).

[46] H. Darcy, *Les fontaines publiques de la ville de Dijon* (Victor Dalmont, Paris, 1856).

[47] M. Reiner, The Deborah Number, Physics today **17**, 62 (1964).

[48] P. A. Cundall and O. D. Strack, A discrete numerical model for granular assemblies, Geotechnique **29.1**, 47 (1979).

[49] E. G. Flekkøy, A. Malthe-sørenssen, and J. Bjørn, Modeling hydrofracture, Journal of Geophysical Research **107**, ECV (2002).

[50] Ø. Johnsen, R. Toussaint, K. J. Måløy, and E. G. Flekkøy, Pattern formation during air injection into granular materials confined in a circular Hele-Shaw cell, Physical Review E **74**, 011301 (2006).

[51] J. L. Vinningland, Ø. Johnsen, E. G. Flekkøy, R. Toussaint, and K. J. Måløy, Granular Rayleigh-Taylor Instability: Experiments and Simulations, Physical Review Letters **99**, 048001 (2007), arXiv:arXiv:0706.0122v2.

[52] J. L. Vinningland, Ø. Johnsen, E. G. Flekkøy, R. Toussaint, and K. J. Måløy, Experiments and simulations of a gravitational granular flow instability, Physical Review E **76**, 051306 (2007).

[53] J. L. Vinningland, Ø. Johnsen, E. G. Flekkøy, R. Toussaint, and K. J. Måløy, Size invariance of the granular Rayleigh-Taylor instability, Physical Review E **81**, 041308 (2010).

[54] M. J. Niebling, E. G. Flekkøy, K. J. Måløy, and R. Toussaint, Mixing of a granular layer falling through a fluid, Physical Review E **82**, 011301 (2010).

[55] M. J. Niebling, E. G. Flekkøy, K. J. Måløy, and R. Toussaint, Sedimentation instabilities: Impact of the fluid compressibility and viscosity, Physical Review E **82**, 051302 (2010).

[56] J. L. Vinningland, R. Toussaint, M. Niebling, E. G. Flekkøy, and K. J. Måløy, Family-Viscek scaling of detachment fronts in Granular Rayleigh-Taylor instabilities during sedimentating granular / fluid flows, The European Physical Journal Special Topics **204**, 27 (2012), arXiv:arXiv:1207.2974v1.

[57] M. J. Niebling, R. Toussaint, E. G. Flekkøy, and K. J. Måløy, Dynamic aerofracture of dense granular packings, Physical Review E **86**, 061315 (2012).

[58] M. J. Niebling, R. Toussaint, E. G. Flekkøy, and K. J. Måløy, Numerical studies of aerofracures in porous media, Revista Cubana de Fisica **29**, 1E66 (2012),

arXiv:arXiv:1209.2600v1.

[59] L. Goren, R. Toussaint, E. Aharonov, D. W. Sparks, and E. Flekkøy, A General Criterion for Liquefaction in Granular Layers with Heterogeneous Pore Pressure, in *Poromechanics V: Proceedings of the Fifth Biot Conference on Poromechanics* (2013) pp. 415–424.

[60] E. Aharonov, L. Goren, D. W. Sparks, and R. Toussaint, Localization of Shear in Saturated Granular Media : Insights from a Multi-Scaled Granular-Fluid Model, in *Poromechanics V: Proceedings of the Fifth Biot Conference on Poromechanics* (2013) pp. 471–480.

[61] I. Ghani, D. Koehn, R. Toussaint, and C. W. Passchier, Dynamic Development of Hydrofracture, Pure and Applied Geophysics **170**, 1685 (2013).

[62] A. Vass, D. Koehn, I. Ghani, S. Piazolo, R. Toussaint, and A. Vass, The importance of fracture-healing on the deformation of fluid-filled layered systems, Journal of Strctural Geology **67**, 94 (2014).

[63] I. Ghani, D. Koehn, R. Toussaint, and C. W. Passchier, Dynamics of hydrofracturing and permeability evolution in layered reservoirs, Frontiers in Physics **3**, 1 (2015).

[64] E. Bendror and L. Goren, Controls over sediment flux along soil-mantled hillslopes : Insights from granular dynamics simulations, Journal of Geophysical Research Earth Surface **123**, 924 (2018).

[65] S. Ben-Zeev, L. Goren, S. Parez, R. Toussaint, C. Clement, and E. Aharonov, The Combined Effect of Buoyancy and Excess Pore Pressure in Facilitating Soil Liquefaction, in *Poromechanics V: Proceedings of the Fifth Biot Conference on Poromechanics* (2017) pp. 107–116.

[66] C. Clément, R. Toussaint, M. Stojanova, and E. Aharonov, Sinking during earthquakes : Critical acceleration criteria control drained soil liquefaction, Physical Review E **97**, 022905 (2018).

[67] P. C. Carman, Fluid flow through granular beds, Trans. Inst. Chem. Eng. **15**, 150 (1937).

[68] N. Makedonska, D. W. Sparks, E. Aharonov, and L. Goren, Friction versus dilation revisited : Insights from theoretical and numerical models, Journal of Geophysical Research Atmospheres **116**, 1 (2011).

[69] J. G. Berryman, Random close packing of hard spheres and disks, Physical Review A **27**, 1053 (1983).

[70] T. L. Holzer, T. L. Youd, and T. C. Hanks, Dynamics of liquefaction during the 1987 superstition hills, california, earthquake, Science **244**, 56 (1989).

[71] National Academies of Sciences, Engineering and Medicine, *State of the Art and Practice in the Assessment of Earthquake-Induced Soil Liquefaction and Its Consequences* (The National Academies Press, Washington, DC, 2016).